Effect of Nozzle Geometry on the Space-Time Emission of Screech Tones

David Morata* and Dimitri Papamoschou.†
University of California, Irvine, Irvine, CA, 92607

The effect of small-sized conical reflectors on the screech emission of supersonic under-expanded jets was studied experimentally. The investigation focused on two closely spaced fully-expanded Mach numbers, M_j=1.32 and 1.34, and included reflectors with four cone half-angles, from 90° to 60°. The acoustic far-field was surveyed by a microphone phased array that included a continuously-scanning microphone, the latter enabling high spatial resolution. The isolated jets contained well-known screech mode B (flapping) and its harmonics. Addition of the reflectors caused significant changes in the modal emission pattern, with mode switching B to C (helical) occurring at M_j =1.34 but not at M_j =1.32. New modes E and F emerge at both Mach numbers when the cone half-angle is 70° or 60°. The tones are generally unsteady, undergoing fluctuations of as much as 5 dB with time. However, some strong tones that result from the reflection are nearly steady-state. The noise source distribution generally elongates with decreasing cone angle of the reflectors. Some modes show clear scattering from the reflectors, while others do not. The study underscores the complexity that initial conditions can impart on the modal structure of screech.

I. Nomenclature

c_∞	=	ambient speed of sound
D	=	nozzle exit diameter
f	=	cyclic frequency
M_j	=	full-expanded Mach number
t	=	time
U_j	=	fully-expanded jet velocity
x	=	axial coordinate
y	=	transverse coordinate
θ	=	polar angle relative to jet axis
λ_s	=	acoustic wavelength of screech emission

II. Introduction

The acoustic emission of imperfectly-expanded supersonic jets contains turbulent mixing noise and noise due to the interaction of turbulence with the shock cells in the jet plume. Shock-associated noise has a broadband component and a tonal component referred to as screech. All these sources can influence noise emission, but strong screech tones can increase annoyance as well as cause structural damage to surfaces in the vicinity of the jet, e.g., airframe components near the exhaust of a jet engine. The generation mechanisms of screech tones have been theorized and investigated during the last decades. The feedback loop process that sustains the screech generation was first delineated by Powell [1] who argued that flow disturbances that form at the nozzle lip travel downstream and interact with the shock-cell structure. This interaction leads to the generation of acoustic waves that travel in the upstream direction, eventually reaching the nozzle lip. When they reach the nozzle lip, they excite the shear layer and cause additional disturbances,

*Graduate Student Researcher, Mechanical and Aerospace Engineering, dmoratac@uci.edu, Member AIAA.
†Professor, Mechanical and Aerospace Engineering, dpapamos@uci.edu, Fellow AIAA.

closing the feedback loop. Studies have shown that screech generation occurs at a distance of several shock-cells downstream of the nozzle lip [2], and might even occur at multiple downstream locations [3].

The aeroacoustics community has been interested in predicting the directivity and intensity of screech tones since they were first discovered. In his pioneering work, Norum [4] used Powell's theory of spatially stationary monopoles located at the ends of the shock cells, with a phase difference between them, to determine the peak emission for the screech tones and its harmonics. Norum's approach could predict reasonably well the direction of emission for the fundamental screech tone and the second harmonic for some jet oscillation modes. Since then, multiple experimental measurements have been performed on round and rectangular nozzles [5, 6] to study the screech directivity. In addition, numerical simulations have also proven to be helpful in the analysis of the screech generation and emission [2, 7]. More recently, Tam *et al.* [2] made use of the weakest link theory to predict the main directions of emission for the screech tones and their harmonics. The weakest link theory relates the non-linear instability wave in the jet and the shock-cell structure, and allows for the prediction of the principal directions of screech radiation for the fundamental frequency and the harmonics. Predicted emission directions and experimentally measured peak emission directions agree reasonably well for jet oscillation modes A1 (toroidal) and B (flapping).

The geometry upstream of the nozzle exit has been shown to enhance or reduce the screech tone levels. Raman *et al.* [8] studied the feedback and receptivity of screech in a rectangular nozzle by using a circular reflector positioned upstream of the nozzle exit. They showed how the reflector plate changes the location of the pressure node or anti-node of the standing wave pattern in the vicinity of the nozzle exit. This translates into a screech enhancement or reduction, as captured by near-field microphones. More complex geometries such as spherical reflectors have also been investigated [9]. A number of additional experiments have shown how the geometry at the vicinity of the nozzle exit strongly influences the screech feedback loop, even causing mode switching or screech cessation and reactivation [10].

The unsteady behavior of screech tones has been previously investigated using a variety of techniques. Raman [11] performed a periodogram analysis of multiple screech tones to identify modes that are coexisting and modes that are mutually exclusive. Chen *et al.* [12] used the Short-Time Fourier Transform to capture the time-dependence of the screech tones emitted from rectangular nozzles with different aspect ratios. Walker *et al.* [13] used the Morlet wavelet transform to investigate the multiple screech tones emitted from a convergent-divergent nozzle operated at off-design conditions. Berman *et al.* [14] also used a wavelet transform to detect the screech mode switching. A general finding of these studies is that the unsteadiness of screech tones is associated with a decrease in the strength of some of the shock cells responsible for the screech generation. The appearance of weaker and competing modes has also been related to changes in the shock cell strength.

This work investigates the effect of conical reflectors, placed around the nozzle exit, on the space-time emission of screech noise from an underexpanded jet issuing from a convergent nozzle. The modal content, directivity, and unsteadiness of the screech tones are investigated at four cone angles and two fully-expanded jet Mach numbers. The investigative tools comprise conventional sound pressure level spectra, short-time spectra, and beamforming. In addition to microphones fixed in space, a continuously-scanning microphone allows high spatial resolution in the assessments of tonal directivity and source location from the beamforming maps.

III. Experimental Setup

A. Phased Microphone Array

Noise measurements were conducted in the UCI Aeroacoustics Facility depicted in Figs. 1 and 2. The microphone array comprises twenty-four 1/8-inch condenser microphones (Brüel and Kjaer, Model 4138) with frequency response up to 120 kHz. The microphones are connected, in groups of four, to six conditioning amplifiers (Brüel and Kjaer, Model 2690-A-0S4). The outputs of the amplifiers are sampled simultaneously, at 250 kHz per channel, by three 8-channel multi-function data acquisition boards (National Instruments PCI-6143) installed in a computer with an Intel i7-7700K quad-core processor. National Instruments Labview software provides the interface for signal acquisition and filtering, as well as control of the experiment. The microphone signals were conditioned with a high-pass filter set at 350 Hz to remove any spurious noise. Temperature and humidity inside the chamber were recorded to enable the calculation of the effects of atmospheric absorption.

Far-field noise measurements were conducted with the microphones mounted on a linear inclined holder and covering a polar aperture from $\theta = 19°$ to $101°$, with the polar angle θ measured from the jet centerline with reference the nozzle exit (see Fig. 1). The minimum distance from the nozzle exit was $R = 0.9$ m. Twenty-three microphones were fixed and one was scanning continuously along a line very close to the line of the fixed sensors. The scanning microphone was mounted on a linear traverse consisting of a belt drive (Igus ZLW-0630) powered by a servo motor (ClearPath MCPV). The trajectory of the scanning microphone was parallel to the fixed microphone line, with a lateral offset $\Delta z = -6$ mm. The position of the scanning microphone was determined from the encoder signal of the motor (ClearPath MCPV) powering the traverse and verified by a laser displacement sensor (SICK OD1000). The servo was programmed to rotate at fixed revolutions per minute with a velocity ramp-up and ramp-down to prevent damage to the scanning microphone. The steady-state speed was of 75.94 mm/s, with a stroke length of 900 mm. A total of 3×10^6 samples were acquired for each channel, corresponding to an acquisition time of 12 s. Further details on the scanning microphone setup can be found in Ref. [15].

Sound Pressure Level (SPL) spectra were computed from the microphone signals using a Fast Fourier Transform (FFT) size of 4096, giving a frequency resolution of 61 Hz. The SPL spectra were corrected for actuator response, microphone free-field correction, and atmospheric absorption. They are referenced to a constant radius of 0.305 m from the nozzle exit.

Beamforming utilized only nine of the fixed microphones in combination with the scanning microphone, as shown in Fig. 3. This arrangement covered the polar sector $55 \leq \theta \leq 101°$, which is relevant to the screech emission of the jet flows considered here. The noise source maps were computed using the Direct Spectral Estimation method of Ref. [15] with the variable block division according to the guidance of Ref. [16]. The noise source is modeled as a linear distribution of uncorrelated monopoles and is obtained by minimizing the difference between the modeled and the measured cross-spectral matrices using a Bayesian inversion approach.

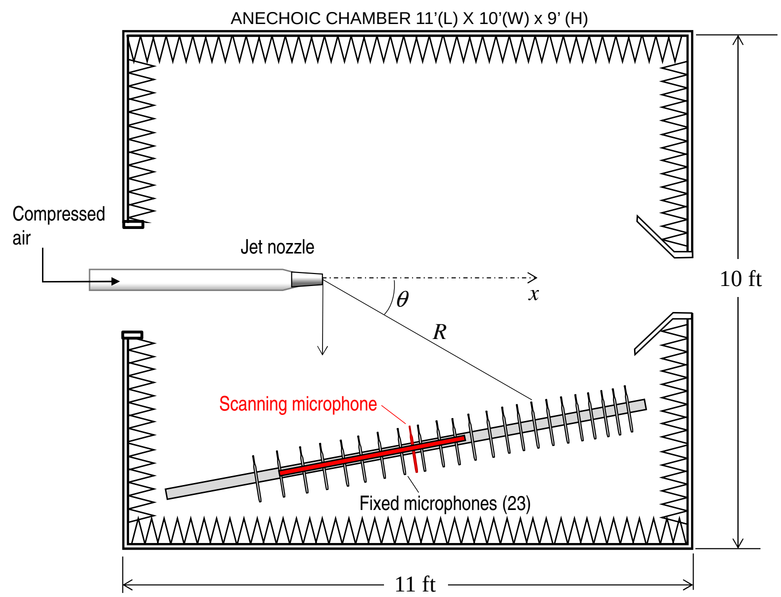

Fig. 1 Diagram of the UCI anechoic chamber. The scanning microphone is indicated in red.

B. Jet Flow

This study examined underexpanded round jets issuing from a convergent nozzle with exit diameter $D = 14.22$ mm and lip thickness of 0.4 mm. The nozzle was supplied by air at room temperature at a variety of total pressures p_0. Conical reflector surfaces were mounted around the exit of the nozzle as depicted in Fig. 4. All the surfaces had the same base diameter of 60.0 mm ($4.22D$) and cone half-angles of 90° (flat plate), 80°, 70°, and 60°. The surfaces were 3D printed using a Formlabs Form 2 printer, and polished so that their surface roughness was much smaller than the screech acoustic wavelength. Structures upstream of the nozzle were covered with anechoic foam to minimize any reflections towards the nozzle (Fig. 2).

Operation of the isolated nozzle (without reflector) at sweep of total pressures, from 239 kPa to 335 kPa, identified strong screech tones within a narrow range of total pressure associated with fully-expanded Mach numbers of $M_j = 1.32$ ($p_0 = 289$ kPa) and $M_j = 1.34$ ($p_0 = 297$ kPa). Consequently, experiments with reflectors were run at these two closely spaced Mach numbers. The corresponding fully-expanded jet velocities were $U_j = 392$ m/s and 397 m/s. The Reynolds

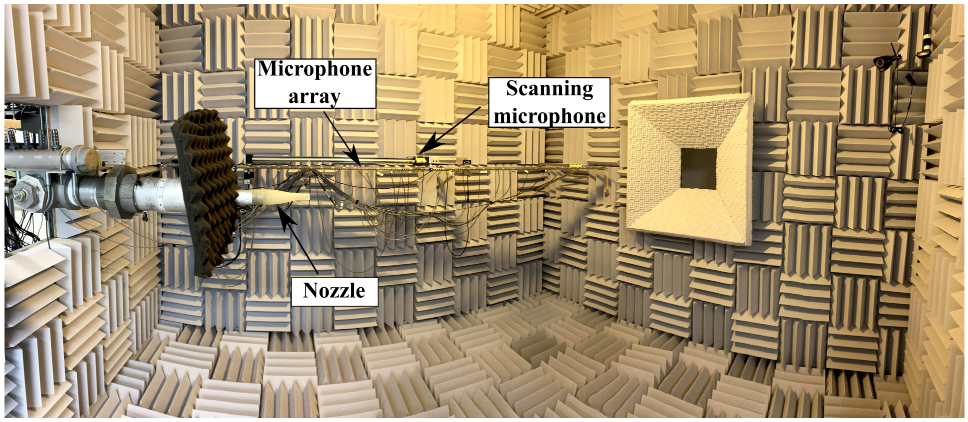

Fig. 2 Photograph of the anechoic chamber. The nozzle, microphone array and scanning sensor are marked.

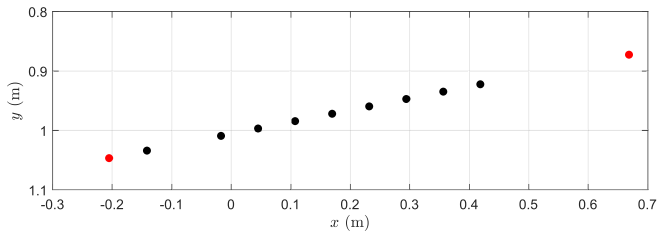

Fig. 3 Coordinates of the fixed sensors (black cicles) and initial and final position of the scanning sensor (red circles) used in beamforming.

number based on nozzle exit diameter was 6.5×10^5 for the average of the two conditions. During each experimental run, the total pressure was held to within 1% of its target value.

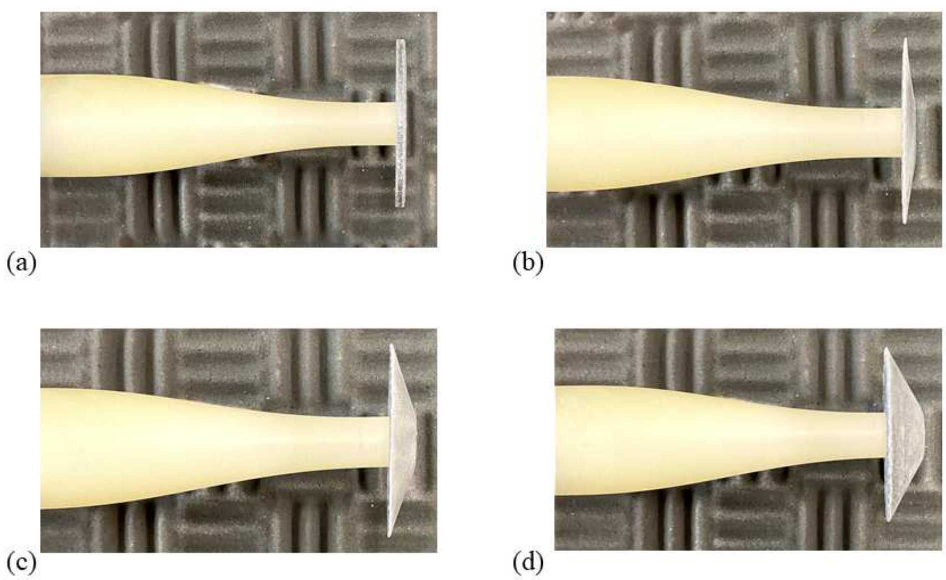

Fig. 4 Photographs of the nozzle and conical reflectors. (a) 90°; **(b)** 80°; **(c)** 70°; **and (d)** 60°.

IV. Results

In the presentation of the results the notation $X^{(n)}$ is used to designate a screech tone, where X is the mode and n is the harmonic. The mode notation of Ref. [17] is followed. Modes A1 and A2 denote torroidal oscillation. Modes B and C describe lateral and helical oscillations, respectively. Reference [17]) also identified an "unknown" mode E as well as a mode that was not labeled.

A. SPL Spectra

SPL spectra are presented based on the full record of the microphone signals (12 s). They will be plotted for polar angle $\theta = 87.4°$, at which one encounters a richness of tones for the various nozzle configurations examined. Figure 5 compares the SPL of the isolated jet with that of the jet with the 90° reflector at M_j=1.34 and 1.32. It is seen that the isolated jet has four prominent tonal components $B^{(1)}$, $B^{(2)}$, $B^{(4)}$ and $B^{(6)}$. The jet at $M_j = 1.34$ with the reflector undergoes a mode switch, with tone $C^{(1)}$ replacing $B^{(1)}$, and tone $C^{(2)}$ partially replacing $B^{(2)}$. Tone $F^{(1)}$ is also seen and appears to result from the interaction between $B^{(1)}$ and $C^{(1)}$. Its frequency follows approximately $f_{F^{(1)}} \approx f_{B^{(1)}} + f_{C^{(1)}}$. This behavior has been seen before in rectangular jets [18, 19] and is the result of a nonlinear phase locking between tones and multiple instability modes present in the shear layer. The jet at $M_j = 1.32$ does not undergo a mode switch. Tonal emission is enhanced, with harmonics $B^{(1)}$ through $B^{(8)}$ arising. Their frequencies are lower than for the isolated jet, indicating an increase in the shock-cell spacing that increases the screech wavelength. Note that the broadband shock-associated noise source levels are higher for the cases with the reflector.

Figure 6 shows the SPL spectra for the isolated jet and the jet with the 80° reflector. The effects are similar to those for the 90° reflector: a mode switch (from B to C) and emergence of $F^{(1)}$ for $M_j = 1.34$; no mode switch but enhancement of tones for $M_j = 1.32$. The frequency of $F^{(1)}$ again follows $f_{F^{(1)}} \approx f_{B^{(1)}} + f_{C^{(1)}}$.

The results for the 70° reflector are shown in Fig. 7. For $M_j = 1.34$, the reflector causes a partial mode switch with tone $B^{(1)}$ changing to $C^{(1)}$, and the higher harmonics of mode B not being shifted. The reflector effect at $M_j = 1.32$ is different from the previous cone angles. Tone $E^{(1)}$ appears very prominently, $B^{(1)}$ is almost completely suppressed, and $F^{(1)}$ makes a weak appearance with $f_{F^{(1)}} \approx f_{B^{(1)}} + f_{E^{(1)}}$. The latter suggests an interaction between modes B and E. In general, the tones at M_j=1.32 are not uniformly enhanced as with the previous reflectors.

The effect of the 60° reflector on the SPL is seen in Fig. 8. There is no mode switch, but the fundamental tone of mode E becomes prominent at both jet Mach numbers and its second harmonic $E^{(2)}$ (unseen in the previous cases) is now significant. Tone $B^{(1)}$ is practically suppressed at $M_j = 1.34$ and appears weak at $M_j = 1.32$. Tone $F^{(1)}$, at the frequency $f_{F^{(1)}} \approx f_{B^{(1)}} + f_{E^{(1)}}$, appears for both jet Mach numbers. Again, it appears that mode F is the result of interaction of modes B and E. Note that the broadband shock-associated noise is significantly lower with the 60° reflector. The dynamics of this configuration appear quite distinct from those of the higher-angled reflectors.

The results seen in the above figures are summarized in a plot of normalized screech-tone wavelength of the fundemental mode, λ_s/D, versus fully-expanded Mach number M_j, shown in Fig. 9. The plot comprises the present data as well as the data of earlier works [17, 20]. For the present data, the plot includes the full M_j range for the isolated nozzle and the specific investigations of the nozzle with reflectors at $M_j = 1.32$ and 1.34. The screech wavelengths for the isolated jet line up well along mode B (lateral oscillation) of the past works. The reflectors trigger modes C, E, and F, as was seen in the SPL plots. At $M_j = 1.32$, there is no mode switching with the 90° and 80° reflectors, and the tones of mode B are manifested at lower frequency, indicating an increase in the shock-cell spacing; modes E and F appear for the 70° and 60° reflectors. At $M_j = 1.34$, the 90° and 80° reflectors cause mode switching from B to C as well as the emergence of tone $F^{(1)}$; the 70° reflector causes partial mode switching from B to C; and the 60° reflector causes no mode switching and strong emergence of mode E. The screech tones for the 60° reflector are similar at $M_j = 1.32$ and 1.34. Note that the frequencies of the tones of mode B of the jet with the 60° reflector are coincident with those of the isolated jet. For the cases in which mode E and mode B were present, the two fundamental frequencies could be seen at some of the polar stations surveyed. However, when mode B and mode C were present, the fundamental frequency for mode B could not be seen and was inferred from its second harmonic.

To the authors' knowledge, the dynamics of mode E have not been investigated before. The frequencies of what we named mode *F*, which appears due to the complex interaction between modes B and C or B and E, are close to those of the unlabeled mode of Seiner *et. al* [17]. In addition, the dynamics of the generation of modes B/C, E, and F appear to be different, as discussed in next sections.

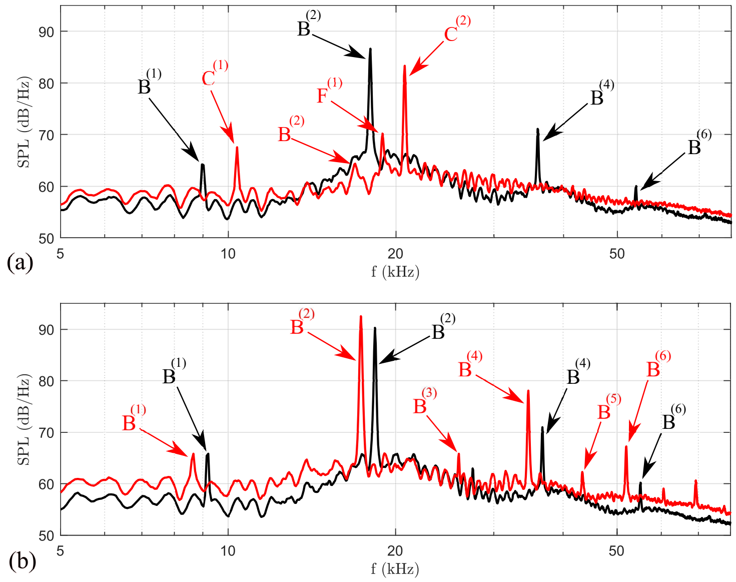

Fig. 5 SPL spectra for the isolated jet (black lines) and the jet with the $90°$ **reflector (red lines). (a)** $M_j = 1.34$**; (b)** $M_j = 1.32$**.**

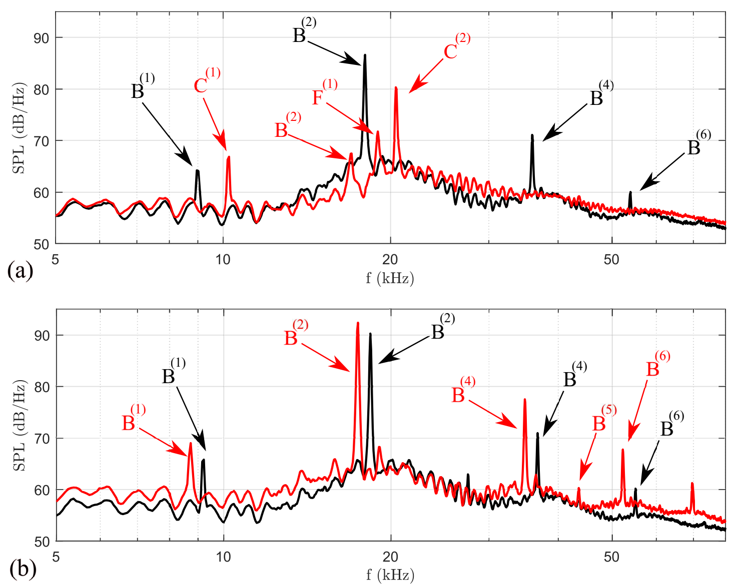

Fig. 6 SPL spectra for the isolated jet (black lines) and the jet with the $80°$ **reflector (red lines). (a)** $M_j = 1.34$**; (b)** $M_j = 1.32$**.**

B. Tone Unsteadiness

We use the "instantaneous" SPL spectra to identify the temporal behavior of screech tones and their interactions, similarly to Ref. [11]. The steps involved in its calculation are summarized as follows. Each microphone signal is divided into 365 blocks with 50% overlap. Each block contains 16384 samples, corresponding to a block time of 0.066 seconds, which defines the temporal resolution. At the fully-expanded jet velocity of $U_j = 394\ m/s$, this translates to a distance of about 1830 jet diameters, which is deemed sufficient to obtain converged statistics. The SPL spectrum is

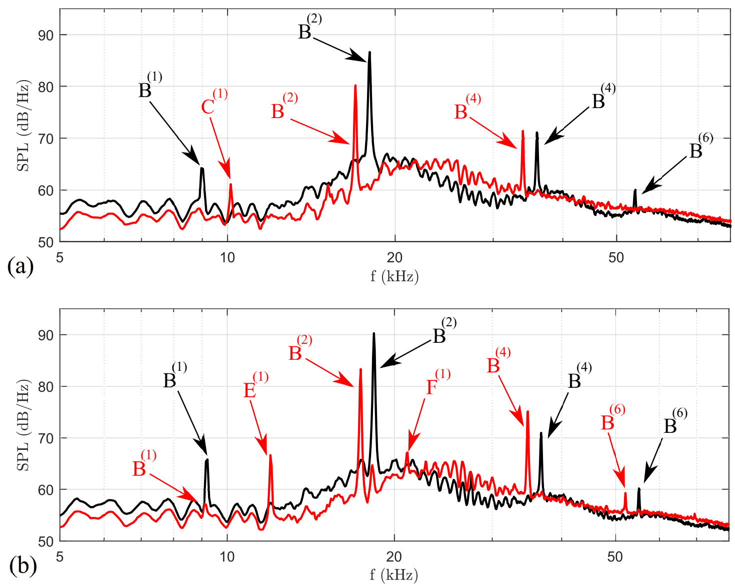

Fig. 7 SPL spectra for the isolated jet (black lines) and the jet with the 70° **reflector (red lines). (a)** $M_j = 1.34$**; (b)** $M_j = 1.32$**.**

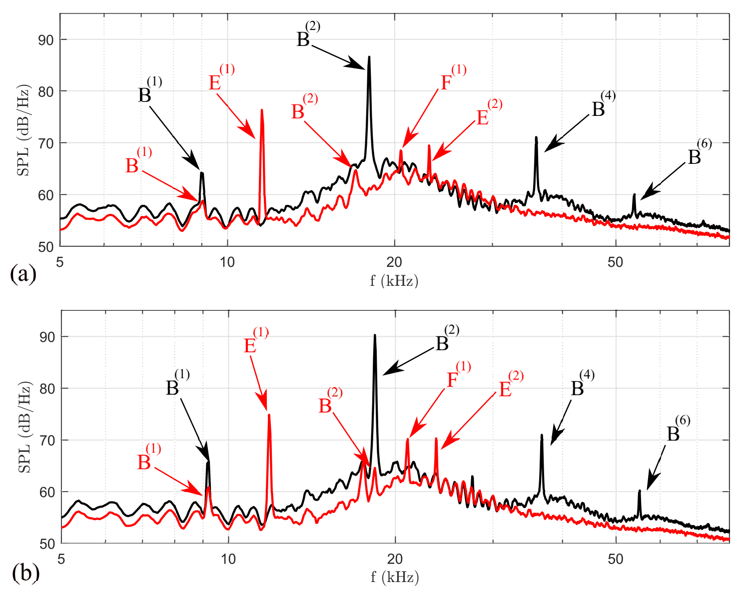

Fig. 8 SPL spectra for the isolated jet (black lines) and the jet with the 60° **reflector (red lines). (a)** $M_j = 1.34$**; (b)** $M_j = 1.32$**.**

computed for each block using an FFT size of 4096, with a frequency bandwidth of 61 Hz. Waterfall plots of SPL versus frequency f and dimensionless time $\frac{t}{D/c_\infty}$ will be presented for $\theta = 87.4^\circ$, the same angle for which the full-record SPL spectra were presented earlier, and for $M_j = 1.32$ and 1.34. The spectra will be plotted for two frequency ranges that contain some of the tones seen in the spectra of Figs. 5-8. Only the first 6 seconds of the experiment will be shown to aid the visualization of the results.

Figure 10 plots the "instantaneous" SPL spectra for the isolated jet and for the jet with the 60° reflector at $M_j = 1.34$.

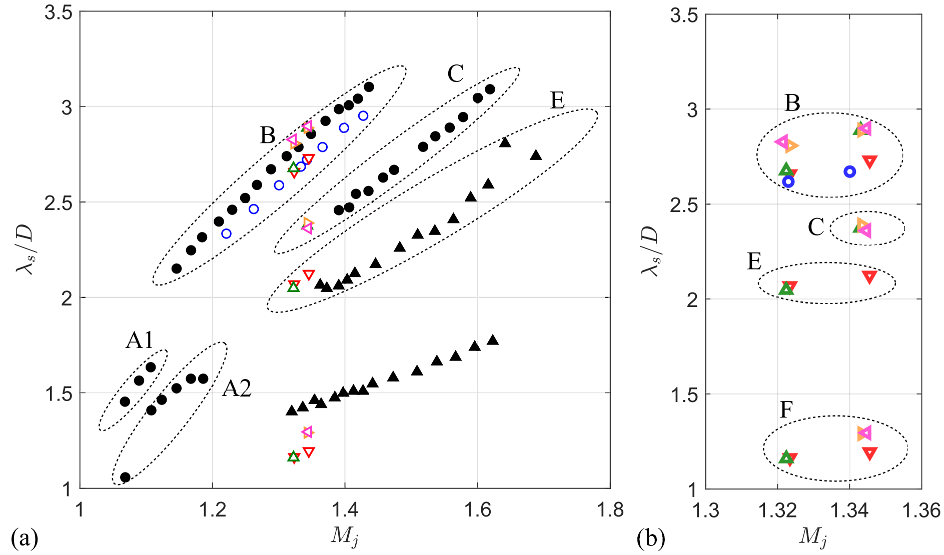

Fig. 9 Normalized screech wavelength versus fully-expanded Mach number for underexpanded jets. (a) Solid circles extracted from Ref. [20]; solid triangles extracted from Ref. [17]; open symbols are for the present experiments: blue for the isolated jet; pink, orange, green, and red for the $90°$, $80°$, $70°$, **and** $60°$ **reflectors, respectively. (b) Close up of the range** $M_j \in [1.30, 1.36]$ **showing only the present measurements.**

For the isolated jet, in the frequency range covered, tones $B^{(1)}$ and $B^{(2)}$ are evident, the latter being significantly stronger. The amplitudes of tone $B^{(2)}$ and $B^{(1)}$ undergo strong variations. With the $60°$ reflector installed tone $B^{(1)}$ is suppressed and tone $E^{(1)}$ emerges at high amplitude and minimal variation with time. Lower-amplitude tones $F^{(1)}$ and $E^{(2)}$ replace $B^{(1)}$ and undergo significant variations with time. No mode switching versus time was noted for any of the configurations covered here at $M_j = 1.32$ and 1.34, with all modes coexisting.

The tone variation with time can be further quantified by evaluating the tonal "energy" for each block. This is done by integrating the power spectral density over a short frequency interval that includes the tone, with reference the broadband level around the tone. The results are presented in the form of an overall sound pressure level (OASPL) and units of decibels. Figure 10 plots the time evolution of OASPL for tones $B^{(1)}$ and $B^{(2)}$ for the isolated jet; and tones $E^{(1)}$ and $E^{(2)}$ of the jet with $60°$ reflector. The tones for the isolated jet undergo significant variations, as much as 5 dB, with time. Preliminary spectral analysis of the OASPL time variation indicates a dominant time scale of ~ 0.25s for the unsteadiness. Installation of the $60°$ reflector triggers the fundamental tone of mode E which is much steadier than tones $B^{(1)}$ and $B^{(2)}$ of the isolated jet. The variation of its second harmonic, $E^{(2)}$ is similar to those of $B^{(1)}$ and $B^{(2)}$. It appears that tone $E^{(1)}$ has little "competition" that would cause unsteadiness. The slight decrease of the amplitude of tones $E^{(1)}$ and $E^{(2)}$ is associated with an increase in the total pressure p_0 of about 1 kPa (0.3%).

C. Tone Directivity

The directivity of the screech tones was investigated using the continuously-scanning sensor. Instantaneous SPL spectra, as defined in the previous section, were used to infer the variation of tone levels versus polar angle with high spatial resolution. The signal of the scanning sensor was divided into 299 blocks with 50% overlap. Each block contained 20000 samples, corresponding to a duration of 0.08 seconds. During this time, the sensor traversed 6.1 mm, yielding an angular resolution $\Delta\theta \approx 0.3°$ for the polar sector covered. A Fast Fourier Transform with size 4096 was used to calculate the SPL spectra. This space-time procedure for producing highly resolved SPL(θ) can be affected by the time intermittency of the tones, discussed in the previous section. It is thus expected that the polar directivity may contain spurious variations due to the tone unsteadiness. Results will be presented as waterfall plots of SPL versus f and θ for fully-expanded Mach numbers $M_j = 1.32$ and 1.34.

Figure 12 presents the directivity of the SPL spectra for the isolated jet. Only mode B is present, with $B^{(2)}$ dominating the highest polar angles for both M_j. The fundamental tone $B^{(1)}$ is present for the enrire polar sector

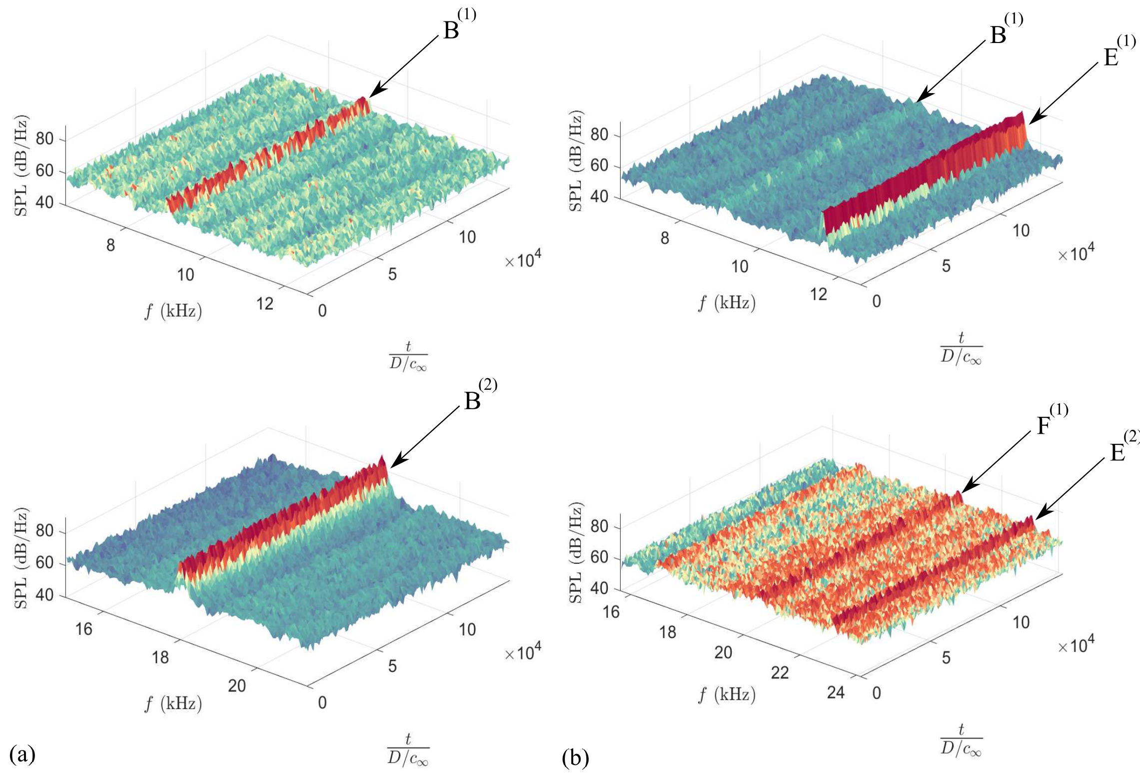

Fig. 10 Instantaneous SPL of (a) the isolated jet and (b) the jet with $60°$ reflector. Both jets are at $M_j = 1.34$ and the polar angle is $\theta = 87.4°$.

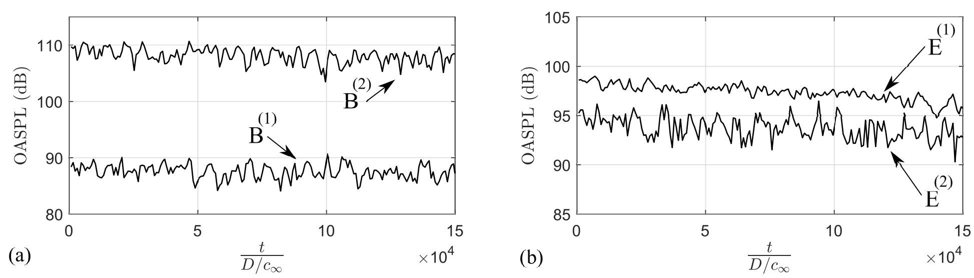

Fig. 11 OASPL versus time for (a) tones $B^{(1)}$ and $B^{(2)}$ of the isolated jet; and (b) tones $E^{(1)}$ and $E^{(2)}$ the jet with $60°$ reflector.

covered and is 15 to 20 dB lower than $B^{(2)}$. This is in line with previous experimental results [2, 4]. The directivity of $B^{(1)}$ appears irregular.

The effect of the 90° reflector is shown in Fig. 13. For $M_j = 1.34$, there is mode switching from B to C; tone $C^{(2)}$ peaks at the highest polar angles while tone $C^{(1)}$ peaks near $\theta = 60°$ and is 10 to 20 dB lower. Tone $F^{(1)}$ appears at the highest polar angles and is about 15 dB lower than $C^{(2)}$. For $M_j = 1.32$, there is no mode switch; the downstream emission of $B^{(1)}$ in enhanced and the directivity of $B^{(2)}$ remains mostly unchanged.

The overall trends for the jet with 80° reflector, shown in Fig. 14, are similar to those of the 90° reflector. The directivity of $C^{(2)}$ and $C^{(1)}$ remain mostly unchanged at $M_j = 1.34$, with tones $B^{(2)}$ and $F^{(1)}$ becoming more prominent.

Figure 15 shows the SPL spectra for the jet with the 70° reflector. For $M_j = 1.34$, modes B and C coexist. Tone

$B^{(1)}$ is not detected in the surveyed polar sector; however, $B^{(2)}$ is very prominent, peaking at the upstream-most angles. Tone $C^{(1)}$ is very weak, peaking near $\theta = 60°$. For $M_j = 1.32$, tone $B^{(2)}$ becomes prominent in the upstream-most directions; tone $E^{(1)}$ emerges in the entire polar sector and peaks near $\theta = 50$ to $70°$; and tone $F^{(1)}$ makes a weak appearance and peaks near 90°.

The directivity patters for the jet with 60° reflector, shown in Fig. 16 are similar for the two Mach numbers. Modes B and E coexist, the latter producing a very prominent $E^{(1)}$ tone throughout the polar sector. Tone $E^{(2)}$ appears for $\theta > 75°$ at lower levels than $E^{(1)}$. Tone $F^{(1)}$ is present and peaks near 90°. Tone $B^{(1)}$ is very weak but is present throughout the polar sector. Tone $B^{(2)}$ peaks near $\theta = 90°$ for both cases.

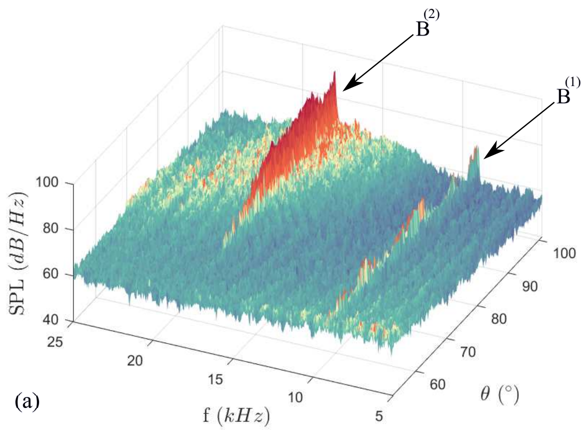

Fig. 12 Directivity of SPL for the isolated jet (a) $M_j = 1.34$**; (b)** $M_j = 1.32$**.**

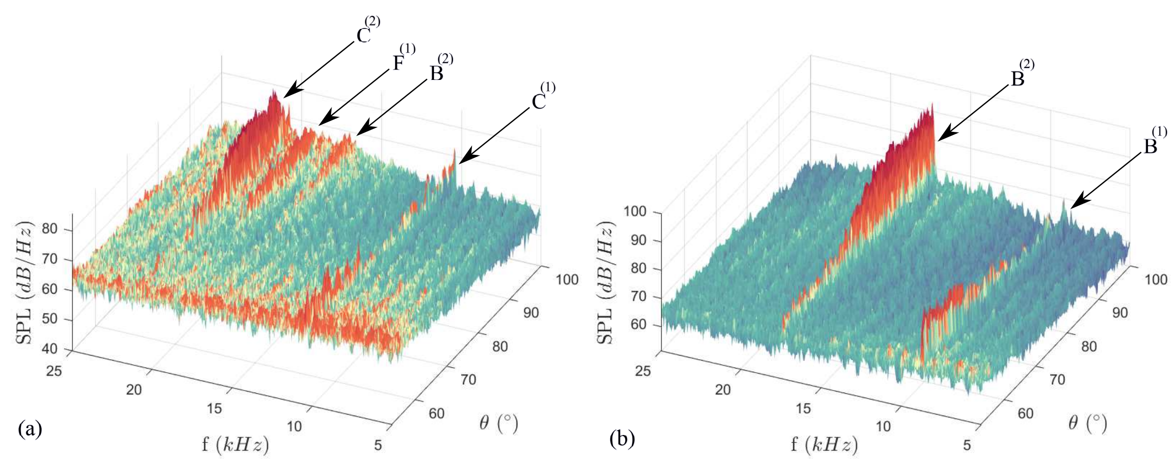

Fig. 13 Directivity of SPL for the jet with the $90°$ **reflector. (a)** $M_j = 1.34$**; (b)** $M_j = 1.32$**.**

Some general directivity trends are inferred from the results presented. Tones $B^{(2)}$ and $C^{(2)}$ radiate at large polar angles, starting at about $\theta = 80°$. If mode E is present, its fundamental tone $E^{(1)}$ is measured throughout the polar sector and its second harmonic $E^{(2)}$ is present for $\theta > 70°$. Tone $F^{(1)}$ peaks near $\theta = 90°$, independently of the reflector or the jet Mach number.

D. Beamforming

The beamforming method described in Section III.A allows measurement of the space-frequency distribution of the noise source with high spatial resolution. The source distribution $\psi(x, f)$ is *coherence-based*. At a given frequency, it

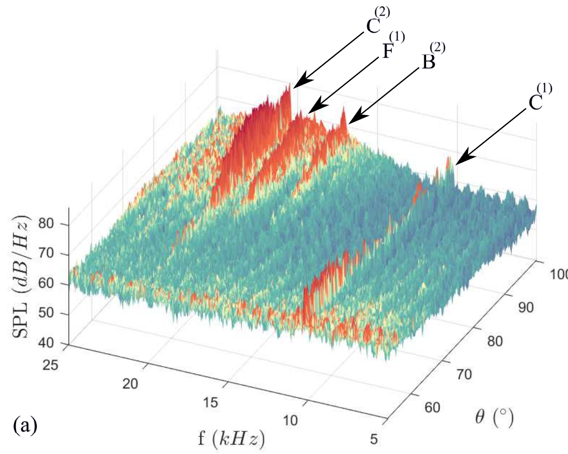

Fig. 14 Directivity of SPL for the jet with the 80° **reflector. (a)** $M_j = 1.34$**; (b)** $M_j = 1.32$**.**

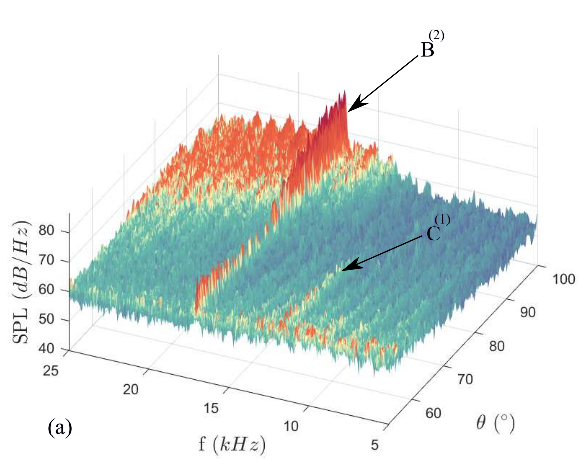

Fig. 15 Directivity of SPL for the jet with the 70° **reflector. (a)** $M_j = 1.34$**; (b)** $M_j = 1.32$**.**

satisfies $\int \psi(x)dx = 1$, where the integration covers the entire source region. As such, it portrays the *relative* strength of sources at a given frequency, but not the absolute level. All the results shown here pertain to the jet at $M_j = 1.34$, which underwent mode switching for several of the reflectors used.

Figure 17 plots the noise source distributions for the jets at $M_j = 1.34$ versus x and f. The nozzle exit and the reflection surfaces are located at approximately $x = 0$ m. Thin horizontal layers containing periodic-like patterns represent the locations of screech tones. In the high-frequency region of the plots ($f > 30$ kHz) periodic vertical streaks, starting at $x = 0$ m, are evident for all the jets. Their spacing is approximately one nozzle diameter and they are discernible to about $x/D = 6$. These "shock sources" are associated with the turbulence that is being convected downstream interacting with the shock cell structure of the jet. This pattern has been seen to be approximately aligned with the tips of the shock cells in Breen and Ahuja [21]. The high-frequency source region occupies approximately $8D$ for the isolated jet and the jet with 90° reflector, and spreads to as much as $11D$ with decreasing cone angle of the reflector. This suggests distinct flow dynamics as the reflector angle decreases. In the mid-frequency range ($20 \le f \le 30$ kHz), the reflectors cause a pattern where the source shifts downstream with increasing frequency, the pattern becoming more pronounced with decreasing cone angle. The low-frequency range $f < 20$ kHz contains the fundamental tones of modes B, C, and E. A weak source near $x = 0$ occurs for the isolated jet near 9 kHz. It is associated with the interaction of the upstream-propagating waves of tone $\mathrm{B}^{(1)}$ with the nozzle lip. Stronger sources near $x = 0$ are seen for the 90° and 80° reflector near 10 kHz, corresponding to the reflection of tone $\mathrm{C}^{(1)}$ from the surfaces.

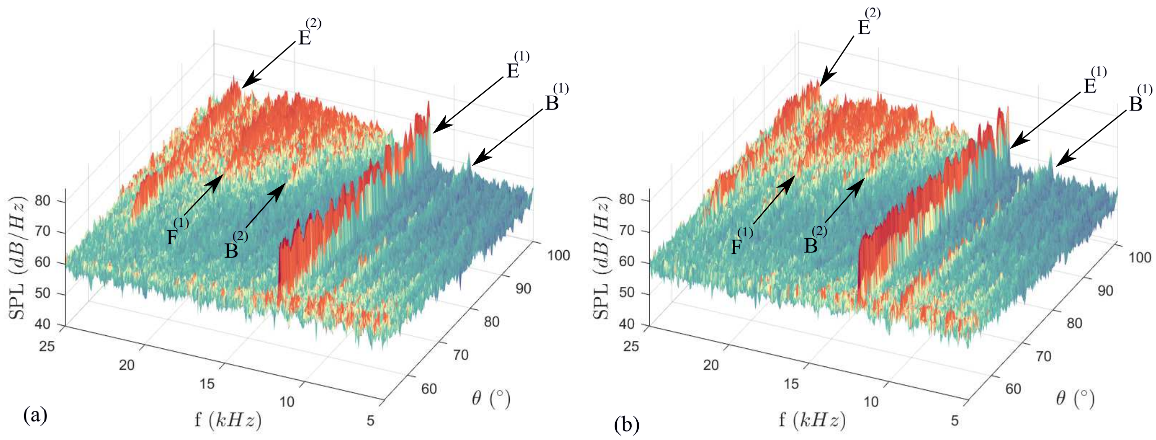

Fig. 16 Directivity of SPL for the jet with the $60°$ reflector. (a) $M_j = 1.34$; (b) $M_j = 1.32$.

Significant sources associated with the reflection from the surfaces near $x = 0$ are seen for frequencies between 9 and 18 kHz for the 70° and 60° reflectors, hinting the presence of additional upstream-propagating components for those configurations.

It is instructive to examine the source distributions for modes B, C, E and F. The source is presented normalized by its maximum value ψ_M. Figure 18 plots the normalized source distribution for tones $B^{(1)}$ and $B^{(2)}$ for the isolated jet and the jet with the 60° reflector. Periodic sources are evident for $B^{(1)}$ of the isolated jet, extending from upstream of the nozzle exit to $x/D = 20$. A localized peak near $x/D = 0$ marks the reflection from the nozzle lip. The upstream sources may be "ghost" phenomena discussed at the end of this section. Installation of the 60° reflector causes a large peak in the distribution of $B^{(1)}$ near $x/D = -1$, corresponding to the edge of the cone, and a weak quasi-periodic pattern downstream. The source for tone $B^{(2)}$ for the isolated jet is centered near $x/D = 6$ and no reflection is apparent, suggesting that this tone lacks upstream-traveling waves. The 60° reflector suppresses completely $B^{(2)}$, so it is not shown.

The source distributions for tones $C^{(1)}$ and $C^{(2)}$ are examined in Fig. 19 for the jet with 90° and 80° reflectors. For both reflectors, the source of $C^{(1)}$ undergoes periodic oscillations that peak near $x/D = 0$, in the vicinity of the reflectors, and decay rapidly downstream. Tone $C^{(2)}$ is centered at $x/D = 5$ and no significant reflections are noted.

Figure 20 plots the source distribution for tone $E^{(1)}$ for the 60° reflector. A very sharp peak is noted near x/D = -1.5, corresponding to the edge of the 60° cone, approximately. This indicates the presence of upstream-propagating waves that reach the reflector and close the feedback loop mechanism for this mode. Periodic oscillations at a much lower level occur downstream. The strong periodic patterns seen for modes $B^{(1)}$ and $C^{(1)}$ are absent in mode E. Examination of the source distribution of $E^{(1)}$ in the other cases of this study shows a similar pattern as that plotted in Fig. 20, indicating that this mode has different dynamics compared to modes B or C.

Figure 21 plots the source distribution for tone $F^{(1)}$ for the jet with the 90° and 80° reflectors. Recall that tone $F^{(1)}$ appeared to be the product of the complex interaction between modes B and C or modes B and E for the 90° and 80° reflectors, respectively. Peak generation for this tone is centered around x/D = 6. There are no sources near$x/D = 0$, indicating that there are no upstream-propagating waves associated with this tone.

The periodic sources seen for tones $B^{(1)}$ and $C^{(1)}$ have been observed earlier in the beamformed maps of an underexpanded jet by Dougherty and Podboy [22] and in the acoustic source images of an overexpanded jet by Papamoschou *et al.* [15]. A weak part of the periodic pattern has been observed at downstream stations where no significant screech generation is expected. The presence of these sources has been named before as "ghost sources". It is not known whether these sources are real or are an artifact of the beamforming approach. Their appearance may be related to the coherent nature of screech. Even though wave synchronization from multiple sources is not a necessary requirement of screech, coherence has been experimentally detected by Ref. [3]. In addition, Powell's original hypothesis of screech [1], which required the waves from downstream sources had to synchronize with those of the upstream sources, is accurate at predicting screech tones at some conditions, indicating wave synchronization might be an important component in screech frequency selection. Edgington-Mitchell *et. al.* [3] have seen how screech

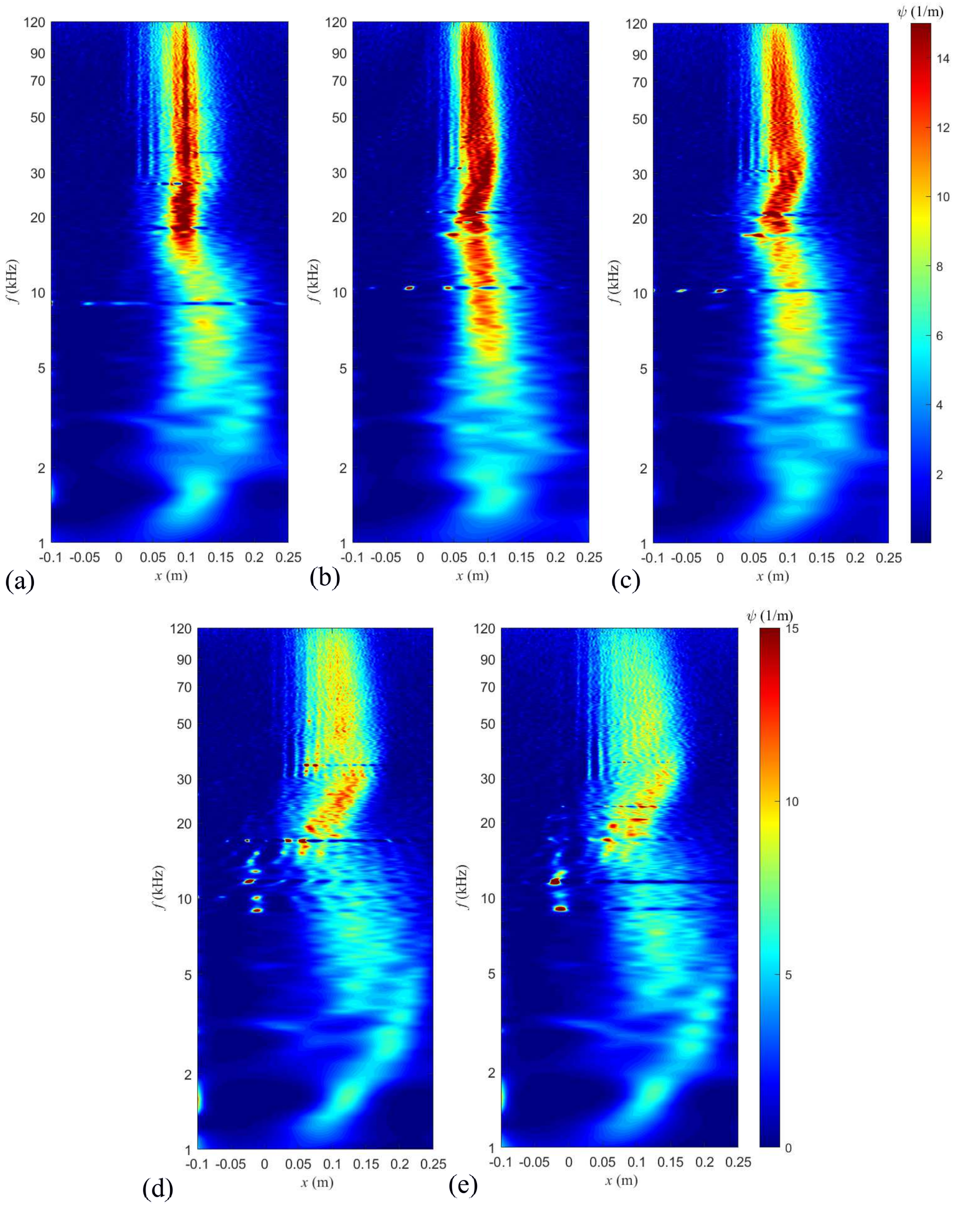

Fig. 17 Coherence-based noise source distribution ψ for the $M_j = 1.34$ jet. (a) Isolated jet. Jets with reflector angles of (b) 90°; **(c)** 80°; **(d)**70°; **and (e)** 60°.

tones are generated through shock leakage at multiple axial stations. If screech emission from the shock-cell tips is coherent (or synchronized), the beamforming process will incorrectly localize the noise sources, and "ghost sources" might appear. However, this argument is difficult to validate from the beamforming results alone and additional data are required. A different beamforming approach that allows for the imaging of coherent noise sources such as DAMAS-C [23] or LORE [24] could shed some light into this problem. Future research will consider such methods.

V. Conclusions

This experimental investigation examined the effect of nozzle initial conditions, in the form of small-sized conical reflectors with variable angle, on the screech emission of underexpanded jets issuing from a convergent nozzle. The

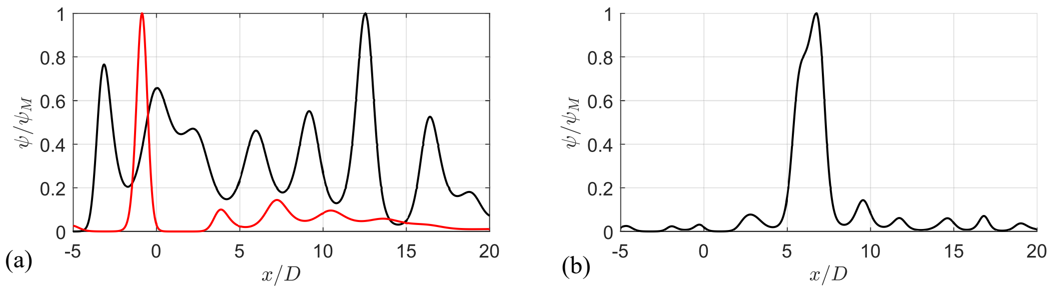

Fig. 18 Normalized coherence-based noise source distributions for the $M_j = 1.34$ isolated jet (black) and with the $60°$ reflector (red). (a) Tone B$^{(1)}$; and (b) tone B$^{(2)}$.

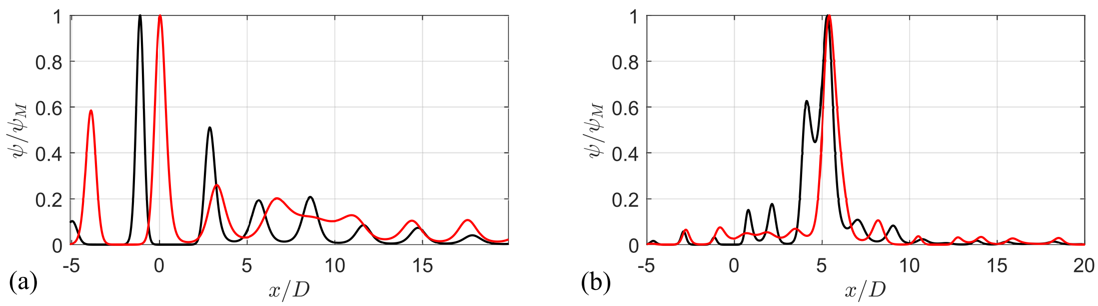

Fig. 19 Normalized coherence-based noise source distributions for the $M_j = 1.34$ jet with the $90°$ (black) and $80°$ (red) reflectors. (a) Tone C$^{(1)}$; and (b) Tone C$^{(2)}$.

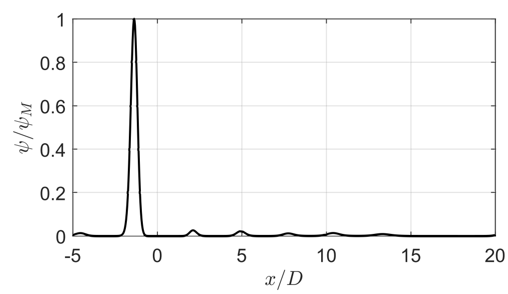

Fig. 20 Normalized coherence-based noise source distribution of tone E$^{(1)}$ for the $M_j = 1.34$ jet with $60°$ reflector.

investigation focused on two closely spaced fully-expanded Mach numbers, $M_j = 1.32$ and 1.34. The acoustic far-field of the jet was surveyed by a microphone phased array that included a continuously-scanning microphone. The latter enabled high-spatial resolution in evaluating the directivity of sound emission and in assessing the source distribution via beamforming.

The isolated jets contain well-known screech mode B. Addition of the reflectors causes significant changes in the modal emission pattern, with mode switching B to C occurring at $M_j = 1.34$ but not at $M_j = 1.32$ for cone angle $90°$ or $80°$. New modes E and F emerged at both Mach numbers when the cone angle is $60°$. The tones are generally unsteady, undergoing fluctuations of as much as 5 dB with time. However, a strong tone E$^{(1)}$ that emerges with the $60°$ reflector is nearly steady-state. The directivity of the tones displays a rich pattern, with the most intense tones peaking near $\theta = 90°$. The noise source maps show distinct sources associated with the shock-cell structure of the jet. The

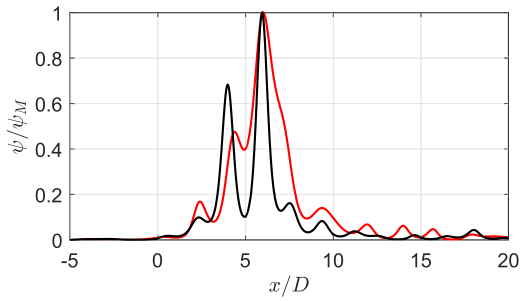

Fig. 21 Normalized coherence-based noise source distribution of tone F$^{(1)}$ for the $M_j = 1.34$ jet with the 90° (black) and 80° (red) reflectors.

noise source generally elongates with decreasing cone angle of the reflector. The source distributions of some tones show clear peaks near the reflectors, indicating the scattering of upstream-propagated waves. However other tones do not show any scattering from the reflectors, suggesting the lack of upstream-traveling waves. It is noteworthy that conical reflectors can in fact reduce screech noise, as is evident in Fig. 8.

More generally, this study underscores the profound effect that initial conditions can have on screech emission and the sensitivity of the resulting modal structure on the details of the initial condition (here the cone angle) and the jet fully-expanded Mach number.

References

[1] Powell, A., "On the Mechanism of Choked Jet Noise," *Proc. Phys. Soc. London*, Vol. 26, 1953, pp. 1039–1056.

[2] Tam, C. K. W., Parrish, S. A., and Viswanathan, K., "Harmonics of Jet Screech Tones," *AIAA Journal*, Vol. 52, No. 11, 2014, pp. 2471–2479. doi:10.2514/1.J052850.

[3] Edgington-Mitchell, D., Weightman, J., Lock, S., Kirby, R., Nair, V., Soria, J., and Honnery, D., "The Generation of Screech Tones by Shock Leakage," *Journal of Fluid Mechanics*, Vol. 908, 2020. doi:10.1017/jfm.2020.945.

[4] Norum, T. D., "Screech Suppression in Supersonic Jets," *AIAA Journal*, Vol. 21, No. 2, 1983, pp. 235–240. doi:10.2514/3.8059.

[5] Norum, T. D., and Seiner, J. M., "Measurements of the Mean Static Pressure and Far-Field Acoustics of Shock-Containing Supersonic Jets," *NASA Technical Memorandum 84521*, 1982.

[6] Seiner, J., Manning, J., and Ponton, M., "Model and Full Scale Study of Twin Supersonic Plume Resonance," *AIAA Paper 87-244*, 1987. doi:10.2514/6.1987-244.

[7] Shen, H., and Tam, C. K. W., "Three-Dimensional Numerical Simulation of the Jet Screech Phenomenon," *AIAA Journal*, Vol. 40, No. 1, 2002, pp. 33–41. doi:10.2514/3.14995.

[8] Raman, G., Panda, J., and Zaman, K., "Feedback and Receptivity During Jet Screech - Influence of an Upstream Reflector," *AIAA Paper 97-0144*, 1997. doi:10.2514/6.1997-144.

[9] Islam, M. T. K., and Seto, K., "Control of Supersonic Jet Noise with a Spherical Reflector," *The Journal of the Acoustical Society of America*, Vol. 116, No. 4, 2004, pp. 2539–2540. doi:10.1121/1.4785132.

[10] Raman, G., "Cessation of Screech in Underexpanded Jets," *Journal of Fluid Mechanics*, Vol. 336, 1997, pp. 69–90. doi:10.1017/S002211209600451X.

[11] Raman, G., "Screech Rones from Rectangular Jets with Spanwise Oblique Shock-Cell Structures," *Journal of Fluid Mechanics*, Vol. 330, 1997, p. 141–168. doi:10.1017/S0022112096003801.

[12] Chen, Z., Wu, J.-H., Ren, A.-D., and Chen, X., "Mode-Switching and Nonlinear Effects in Supersonic Jet Noise," *AIP Advances*, Vol. 8, No. 1, 2018, p. 015126. doi:10.1063/1.5010829.

[13] Walker, S., Gordeyev, S., and Thomas, F., "A Wavelet Transform Analysis Applied to Unsteady Aspects of Supersonic Jet Screech Resonance," *Experiments in Fluids*, Vol. 22, No. 3, 1997, pp. 229–238. doi:10.1007/s003480050041.

[14] Berman, K., Karon, A. Z., Medda, A., and Ahuja, K. K., "Detection of Screech Mode-Switching Using the Discrete Wavelet Transform," *AIAA Paper 2018-3464*, 2018. doi:10.2514/6.2018-3464.

[15] Papamoschou, D., Morata, D., and Shah, P., "Inverse Acoustic Methodology for Continuous-Scan Phased Arrays," *AIAA Journal*, Vol. 57, No. 12, 2019, pp. 5126–5141. doi:10.2514/1.J058085.

[16] Morata, D., and Papamoschou, D., "Advances in the Direct Spectral Estimation of Aeroacoustic Sources Using Continuous-Scan Phased Arrays," *AIAA Paper 2021-0215*, 2021. doi:10.2514/6.2021-0215.

[17] Seiner, J. M., Manning, J. C., and Ponton, M. K., "Dynamic Pressure Loads Associated with Twin Supersonic Plume Resonance," *AIAA Journal*, Vol. 26, No. 8, 1988, pp. 954–960. doi:10.2514/3.9996.

[18] Walker, S. H., and Thomas, F. O., "Experiments Characterizing Nonlinear Shear Layer Dynamics in a Supersonic Rectangular Jet Undergoing Screech," *Physics of Fluids*, Vol. 9, No. 9, 1997, pp. 2562–2579. doi:10.1063/1.869373.

[19] Thomas, F. O., and Chu, H. C., "Nonlinear Wave Coupling and Subharmonic Resonance in Planar Jet Shear Layer Transition," *Physics of Fluids A: Fluid Dynamics*, Vol. 5, No. 3, 1993, pp. 630–646. doi:10.1063/1.858649.

[20] Ponton, M. K., Seiner, J. M., and Brown, M. C., "Near Field Pressure Fluctuations in the Exit Plane of a Choked Axisymmetric Nozzle," *NASA Technical Memorandum 113137*, 1997.

[21] Breen, N. P., and Ahuja, K. K., "Limitations of Acoustic Beamforming for Accurate Jet Noise Source Location," *AIAA Paper 2020-2603*, 2020. doi:10.2514/6.2020-2603.

[22] Dougherty, R., and Podboy, G., "Improved Phased Array Imaging of a Model Jet," *AIAA Paper 2009-3186*, 2009. doi:10.2514/6.2009-3186.

[23] Brooks, T., and Humphreys, W., "Extension of DAMAS Phased Array Processing for Spatial Coherence Determination (DAMAS-C)," *AIAA Paper 2006-2654*, 2006. doi:10.2514/6.2006-2654.

[24] Ravetta, P. A., Burdisso, R. A., and Ng, W. F., "Noise Source Localization and Optimization of Phased-Array Results," *AIAA Journal*, Vol. 47, No. 11, 2009, pp. 2520–2533. doi:10.2514/1.38073.